Engineering Photonic–Plasmonic Coupling in Metal Nanoparticle Necklaces

Alyssa J. Pasquale,[†] Björn M. Reinhard,[‡] and Luca Dal Negro[†,*]

[†]Department of Electrical and Computer Engineering and Photonics Center, Boston University, 8 Saint Mary's Street, Boston, Massachusetts 02215, United States and
[‡]Department of Chemistry, Boston University, 590 Commonwealth Avenue, Boston, Massachusetts 02215, United States

ABSTRACT In this paper, by combining three-dimensional finite-difference time-domain simulations, dark-field scattering analysis, and surface-enhanced Raman spectroscopy (SERS) we systematically investigate the light-scattering and field localization properties of circular loops of closely spaced gold nanoparticles, or "nanoplasmonic necklaces", fabricated by electron-beam lithography on quartz substrates. In particular, we show that nanoplasmonic necklaces support two hybridized dipolar scattering resonances with polarization-controlled subwavelength localized fields (*i.e.*, electromagnetic hot-spots), whose intensities are optimized by varying the necklace particle diameter and the particle number. Moreover, we show that strong field intensity enhancement is obtained for the particular necklace diameters where loop-localized photonic resonances efficiently couple to the broadband plasmonic modes, enabling a simple design strategy for the optimization of electromagnetic near-fields. Following the proposed approach, we design nanoplasmonic necklaces supporting stronger field intensity enhancement than traditional nanoparticle monomer and dimer arrays. Finally, by performing SERS experiments on nanoplasmonic necklaces coated with a pMA molecular monolayer, we validate the optimization of their near-field properties and demonstrate their potential for plasmon-enhanced spectroscopy and sensing.

KEYWORDS: surface-enhanced Raman scattering · electron-beam lithography · plasmonics · nanoparticles · plasmonic arrays

The ability to engineer sub-wavelength-localized optical fields using metal-dielectric nanostructures drives the development of optical biosensors, molecular probes, subwavelength apertures, nanoscale optical antennas, photon sources, and guiding elements.[1] All these applications greatly benefit from the distinctive resonant properties of metallic thin films,[2] nanoparticles with optimized morphologies,[3] and complex arrays with a tunable degree of structural complexity.[4,5] Compact plasmonic devices have been recently realized using triangular bowtie nanoantennas,[6] nanodisk trimer arrays,[7] cube clusters,[8] core–shell nanoparticles,[9] and a variety of nanoparticle shapes and cluster morphologies.[10–12]

In the context of nanoparticle arrays, metallic nanocylinders have been used extensively for the engineering of plasmonic devices.[4,13,14] In particular, metal nanoparticle dimers exhibit near-field concentration in subwavelength gap regions and significant enhancement of the plasmonic near-field[6] due to strong quasi-static coupling between the localized plasmon modes of the nanoparticles in the dimer. Arrays of metallic dimers have been proposed for localized surface plasmon resonance (LSPR) sensors[15] and surface-enhanced Raman scattering (SERS) applications[8,16] and provide a significant improvement over arrays of isolated nanoparticles (*i.e.*, monomer arrays).[17] However, the electromagnetic intensity enhancement and spatial localization obtained by nanoparticle dimers compared to arrays of single particles is strongly polarization-dependent, and it is almost entirely lost when dimers are not excited by radiation of the proper polarization (*i.e.*, parallel to the dimer axis).[16] Recently, the polarization dependence of the near-fields of plasmonic arrays has been shown to dramatically affect the strength of Raman signals[18] as well as plasmon-enhanced fluorescence,[19] limiting their applicability to biosensing and SERS spectroscopy.[8,16] Therefore, there is a need to develop engineerable plasmon-enhanced sensing platforms that simultaneously offer strong enhancement of optical cross sections, localized field intensities, and polarization insensitivity for a variety of optical sensing and spectroscopic applications.[20]

Recently, nanoparticle cluster aggregates with a high degree of circular symmetry have been investigated in nanoparticle clusters[21] as well as in various "oligomer" configurations, giving rise to Fano-type resonances[22–25] of great interest for applications in LSPR sensing.

In this paper, by combining three-dimensional finite-difference time-domain (3D FDTD) simulations with experimental dark-field and Raman spectroscopy, we systematically investigate the far-field scattering

* Address correspondence to dalnegro@bu.edu.

Received for review May 27, 2011 and accepted July 8, 2011.

Published online July 08, 2011
10.1021/nn201959k

resonances and the near-field properties of plasmonic arrays of gold (Au) nanoparticles arranged in circular arrays with increasing rotational symmetry, here on referred to as "nanoplasmonic necklaces". Finally, we demonstrate the potential of the proposed structures as novel substrates for polarization-insensitive, plasmon-enhanced spectroscopy and Raman sensing over broad-frequency spectra.

RESULTS AND DISCUSSION

Nanoplasmonic Necklaces. Nanoplasmonic necklaces are generated by regularly positioning Au nanocylinders of constant diameter (150 nm) and edge-to-edge separation (25 nm) around circular loops of controlled diameter in such a way that the angle between the centers of each cylinder in the necklace is 360° divided by the number of particles. As a result, by increasing the number of cylinders in the necklace, its diameter and degree of rotational symmetry are also increased.

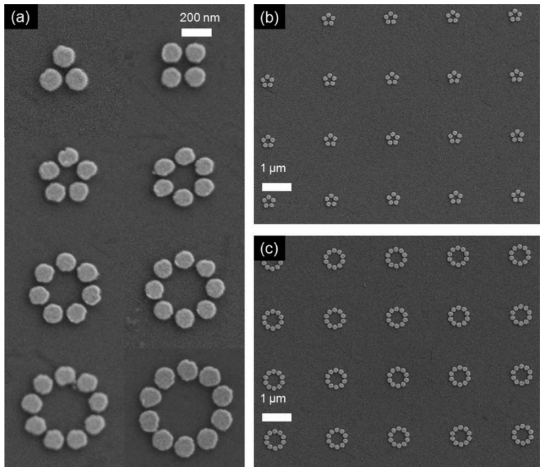

Figure 1. SEM micrographs of nanoplasmonic necklaces. (a) Fabricated necklaces with varying particle numbers. (b) Pentagons and (c) decagons in arrays with center-to-center spacings of 2.5 μm. Each nanoplasmonic necklace consists of gold cylinders of diameter 150 nm and minimum edge-to-edge spacing of 25 nm.

In what follows, we study the far-field scattering and the near-field properties of electromagnetic hotspots as a function of the number of particles in the necklace, the degree of rotational symmetry, and the polarization of the incident field. Furthermore, we demonstrate the role of photonic−plasmonic coupling in the optimization of the optical cross sections and intensity enhancement of nanofabricated plasmonic necklaces, and we utilize dark-field scattering and Raman spectroscopy to validate the numerical results of our analysis.

In Figure 1 we show representative scanning electron micrographs (SEM) of the fabricated nanoplasmonic necklaces on fused silica substrates, demonstrating almost ideal agreement with targeted design parameters. Micrographs of the particle arrays show device consistency over a large pattern area, with each particle array spaced by 100 μm to avoid undesired electromagnetic (diffractive) coupling.

Far-Field Scattering Analysis. In this section, we will focus our computational and experimental analysis on the far-field scattering resonances of nanoplasmonic necklaces.

We show in Figure 2c,d the calculated scattering spectra of nanoplasmonic necklaces of increasing particle number excited using linearly polarized radiation

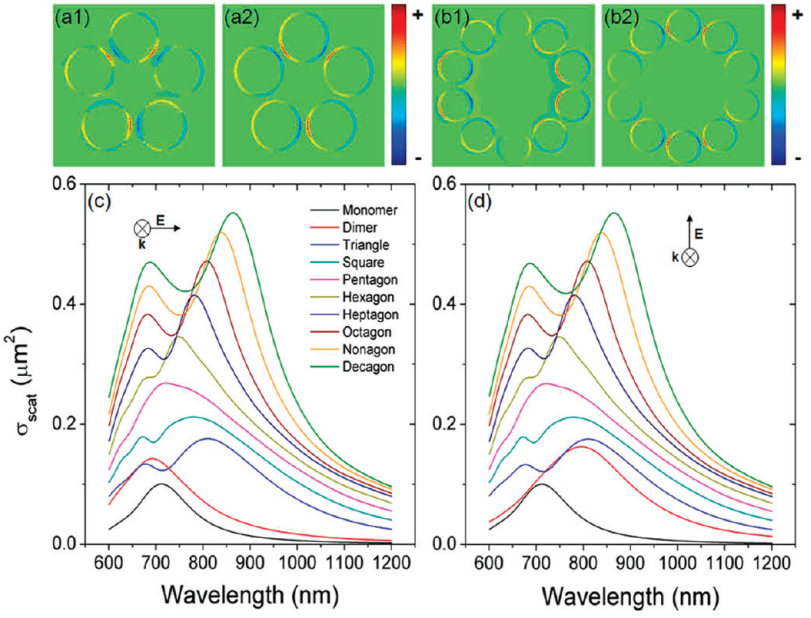

Figure 2. Calculated bound charge densities (excited with 0° incident polarization) of (a1) pentagon low-energy shoulder mode at 634 nm and (a2) at the wavelength of peak scattering (721 nm); (b1) decagon high-energy mode at 688 nm and (b2) low-energy mode at 863 nm. Calculated far-field scattering cross section spectra of nanoplasmonic necklaces at (c) 0° (*x*-axis) and (d) 90° (*y*-axis) incident polarization.

with 0° (*i.e.*, horizontal) and 90° (*i.e.*, vertical) polarization angles, respectively. Data on particle monomers and dimers are also included in Figure 2 for comparison. The scattering cross section is calculated by considering the total scattered power transmitted through a cubic region enclosing the nanoplasmonic necklace and normalizing it to the intensity of the source.

Figure 2 demonstrates clearly that by adding particles to the necklace two distinct modes appear, for any given linear incident polarization, in the far-field scattering spectra. It has been recently shown using the symmetry groups of particle trimers,[23] quadrumers,[9] and septamers[22] that these two modes arise due to hybridization of optically active dipolar modes that can be obtained by group-theoretic arguments. Nanoplasmonic necklaces belong to the dihedral point group, specifically D_{nh}, which is characterized by having n-fold rotational symmetry along a principal axis. The h subscript indicates a horizontal mirror plane that is perpendicular to the principal rotation axis.[26]

An analysis of the bound charge density in the necklaces, calculated from the local field $\vec{E}$ using the expression $\rho_b = -\vec{\nabla} \cdot [\varepsilon_0(\varepsilon_r - 1)\vec{E}]$ at the wavelengths of each resonant mode, gives clear insight into the physical nature of these modes. The calculated charge densities are shown in Figure 2 (a1,a2) for the pentagon and (b1,b2) decagon, considered as representative cases. The pentagon is analyzed at (a1) λ = 634 nm, where a weak shoulder occurs in the scattering cross section, and at (a2) the wavelength (λ = 721 nm) of peak scattering. We can see from its charge distribution that the pentagon shoulder mode is quadrupolar and therefore is not optically active. On the other hand, the charge density at the wavelength of peak scattering (λ = 721 nm) describes a large net dipole moment that can couple to incident electromagnetic radiation, giving rise to a broadband "bright" mode. Close to the region of peak scattering (700−800 nm) of the pentagon necklace, we also note the presence of an additional shoulder corresponding to two different dipolar modes in close proximity. Differently from other necklaces, the dipolar pentagon modes are only weakly excited at normal incidence. The decagon is analyzed at the (b1) high-energy mode (λ = 688 nm) and (b2) low-energy mode (λ = 863 nm) corresponding to two dipolar excitations with nonzero net dipole moments. The low-energy mode is stronger in scattering due to its higher net dipole moment compared to the high-energy mode, as can be seen in Figure 2. With the exception of the pentagon as discussed above, all of the nanoplasmonic necklaces (triangle through decagon) support two hybridized dipolar modes which are active in far-field scattering.

Additionally, we notice in Figure 2 that the low-energy mode has a wavelength position that is more sensitive to the number of particles in the necklace than the high-energy mode, which remains relatively

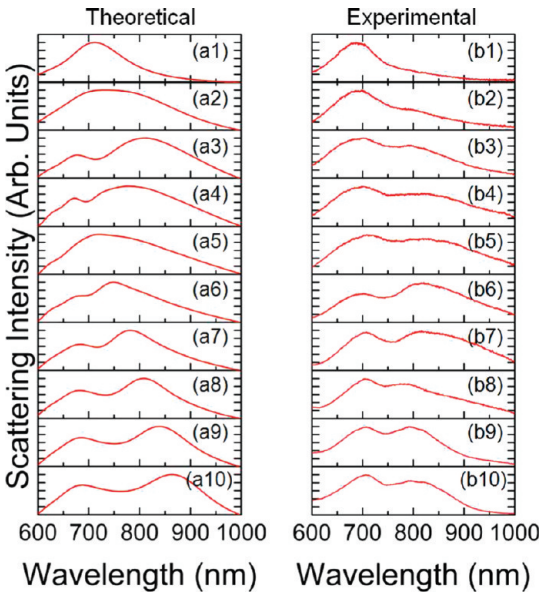

Figure 3. (a1−a10) Calculated scattering cross sections and (b1−b10) experimentally measured dark-field scattering spectra of (a1 and b1) monomers; (a2 and b2) dimers; (a3 and b3) triangles; (a4 and b4) squares; (a5 and b5) pentagons; (a6 and b6) hexagons; (a7 and b7) heptagons; (a8 and b8) octagons; (a9 and b9) nonagons; and (a10 and b10) decagons.

stable in wavelength as more particles are added. This red-shifting of the low-energy mode is consistent with the onset of diffractive coupling effects by increasing the overall necklace diameter, similarly to what is observed in photonic−plasmonic linear gratings.[27] However, in the case of nanoplasmonic necklaces, the minimum interparticle separation remains constant (25 nm) while the overall necklace dimension (its diameter) is increased. Moreover, by comparing the spectra in Figure 2c,d, we notice that the polarization angle of the excitation does not significantly affect the far-field scattering response of nanoplasmonic necklaces in the far-field, as expected on the basis of their high degree of rotational symmetry. On the opposite nanoparticle dimers are very sensitive to the polarization angle and present a shift of over 100 nm in the peak scattering wavelength as the excitation angle is varied from 0° to 90°. In contrast, nanoplasmonic necklaces with hexagonal and higher degree of rotational symmetry are insensitive to the polarization change, with no discernible modification in their far-field scattering spectra.

To confirm the results of our calculations, we measured dark-field scattering transmission spectra of nanofabricated nanoplasmonic necklaces.

We measured necklaces that were patterned in arrays, with each necklace spaced 2.5 μm apart (center-to-center) to avoid photonic coupling between neighboring necklaces.

We show in Figure 3 the experimental scattering spectra for different nanoplasmonic necklaces as well

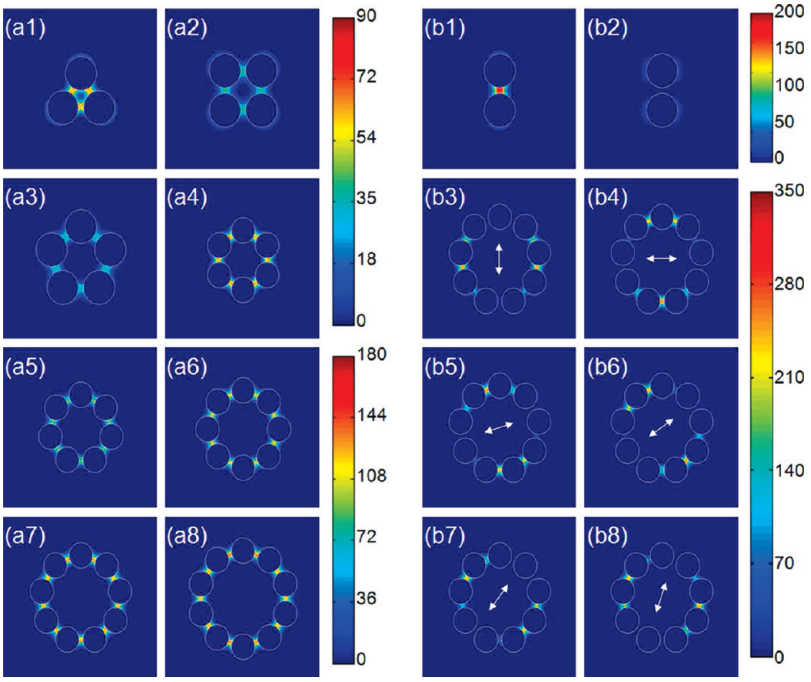

Figure 4. (a) Near-field profiles of nanoplasmonic necklaces excited with unpolarized light with (a1) three through (a8) 10 particles. Near-field profile of the dimer excited at (b1) 90° and (b2) 0°, showing clear polarization dependence of the hot-spots. The nine-particle nonagon excited with polarized light at angles (b3) 90°, (b4) 0°, (b5) 18°, (b6) 36°, (b7) 52°, and (b8) 72° (denoted by the inset arrows) showing the locations of the hot-spots and how they are controlled by the polarization angle.

as monomer and dimer arrays fabricated as a reference. Figure 3 (a1−a10) shows the calculated scattering cross section data under unpolarized excitation for easy comparison with the experimental data in Figure 3 (b1−b10). The measured dark-field scattering spectra of all configurations ranging from monomer (b1) to decagon (b10) are plotted in Figure 3b. Figure 3 indicates remarkable agreement for all the investigated structures between theory and experimental results. Specifically, the presence of two well-defined scattering modes is clearly visible in the scattering spectra. Minor differences between experimental and theoretical spectra can be explained by slight deviations in particle shape and excitation conditions (dark-field experimental setup *vs* normal incidence plane wave in the simulations).

We now turn our attention to a rigorous analysis and design of the near-field properties of nanoplasmonic necklaces, including hot-spot engineering, photonic−plasmonic coupling, near-field lineshapes, and experimental SERS data.

Hot-Spot Engineering. We study the formation, intensity, and spatial location of hot-spots in the nanoplasmonic necklaces as a function of particle number and polarization of the excitation plane wave. In Figure 4 (a1−a8), we show the calculated near-field intensity profiles under unpolarized excitation of the electromagnetic hot-spots as a function of particle number in different necklaces ranging from a three-particle triangle Figure 4 (a1) to a 10-particle decagon configuration Figure 4 (a8). The intensities are shown at the wavelengths corresponding to the peak of the near-field intensity, which varies for each necklace configuration. We observe from Figure 4 (a1−a8) that the number of hot-spots excited in these conditions is equal to the number of particles in the necklace. Despite the fact that the nanoparticles in the different necklaces all have the same diameter (150 nm) and edge-to-edge separation (25 nm), Figure 4 shows that some necklaces produce stronger hot-spot intensity enhancement than others. In particular, there exist optimal necklace dimensions and particle numbers, as we will discuss more in detail below. Here, we emphasize only that due to the predictable hot-spot locations and sensitivity to the particle number, nanoplasmonic necklaces provide a convenient platform for the precise engineering of plasmonic hot-spots.

In Figure 4 (b1−b8) we show the effects of the polarization angle of the incident plane wave on the hot-spot locations and intensities. Without loss of generality, we limit our analysis to the case of a two-particle dimer and a nine-particle nonagon necklace, since similar results have been obtained for all the necklace structures. As expected, the nanoparticle dimer produces an intense hot-spot only when excited along its axis (*i.e.*, longitudinal polarization), while the hot-spot intensity is dramatically decreased when excited with transverse polarization (*i.e.*, perpendicular to the dimer axis). On the contrary, the nonagon necklace supports hot-spots for all polarizations. As expected, the excited hot-spots correspond to the dimers within the necklace that are longitudinally

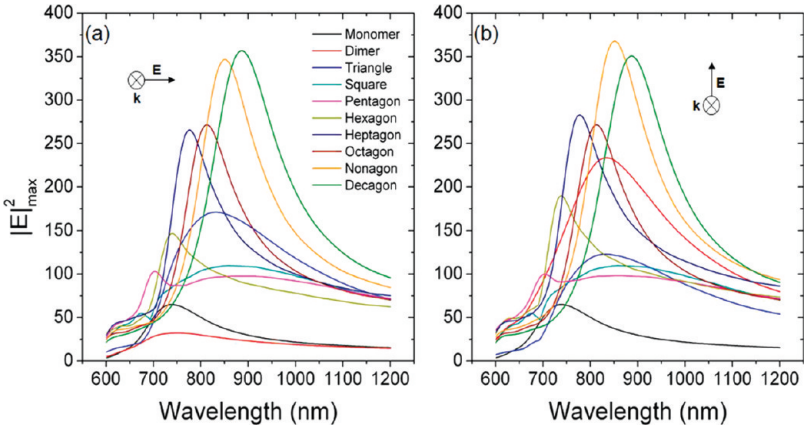

Figure 5. Calculated maximum near-field intensity for nanoplasmonic necklaces of varying particle numbers excited at normal incidence by a plane wave polarized at (a) 0° (*x*-axis) and (b) 90° (*y*-axis).

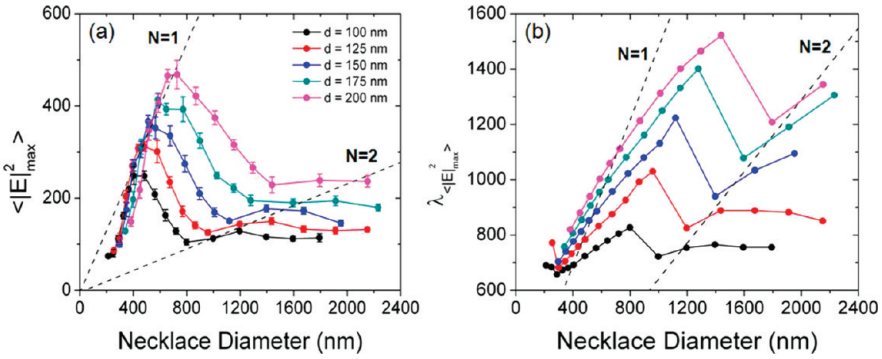

Figure 6. (a) Polarization averaged maximum near-field intensity shown as a function of the overall necklace radius as well as particle diameter. (b) Wavelength of the maximum near-field intensity as a function of overall necklace diameter. Dashed lines in both graphs show the linear fits of the *N* = 1 and *N* = 2 photonic modes.

excited, and their locations rotate within the necklace following the orientation of the incident polarization. In summary, Figure 4 (b3−b8) demonstrates that by varying the polarization angle from (b3) 0° to (b8) 90° in 18° increments, the nonagon necklace always supports more and stronger intensity hot-spots than a dimer, and the hot-spot intensity cannot be suppressed when the polarization angle is changed. Similar results are obtained for all the considered nanoplasmonic necklaces, making them very attractive for sensing applications requiring intense and polarization-insensitive enhancement of plasmonic near-fields.

It is also of great fundamental as well as applied interest for plasmon-enhanced spectroscopy to investigate the wavelength spectra of the plasmon near-field excitations supported by nanoplasmonic necklaces. In Figure 5, we plot the calculated wavelength spectra of the maximum near-field intensity extracted from each necklace configuration. The results shown in Figure 5a are obtained for a polarization angle of 0° and in Figure 5b at a polarization angle of 90° in order to directly compare against the longitudinally polarized dimer case, which is known to produce the strongest field. We see in Figure 5 that the maximum intensities increase with the number of particles in the necklace for both polarizations and also that the near-fields retain high values of intensities over broader wavelength ranges as the particle numbers are increased. We also observe the dramatic effect of polarization sensitivity on the dimer whose maximum intensity is reduced greatly when excited at 0° (off-axis). The simple design of polarization-insensitive plasmonic necklaces with increased hot-spot intensity distributed over large frequency bandwidths can find significant applications in SERS spectroscopy, since many SERS applications require the ability to engineer strong near-fields at both the excitation and Stokes-shifted wavelengths, leading to maximum SERS signals.[28] Finally, it is evident from Figure 5 that the peak wavelengths of the near-field maxima shift to longer wavelengths by adding particles to the necklace, clearly indicating the important role played by photonic diffraction and coupling effects.

Plasmonic−Photonic Coupling. We now discuss the role of photonic coupling effects in nanoplasmonic necklaces associated with their circular resonator structure, and we show that photonic trapping effects enhance plasmonic near-field intensities at well-defined necklace diameters.

The results of our analysis are shown in Figure 6. In Figure 6a we show the average value of the maximum

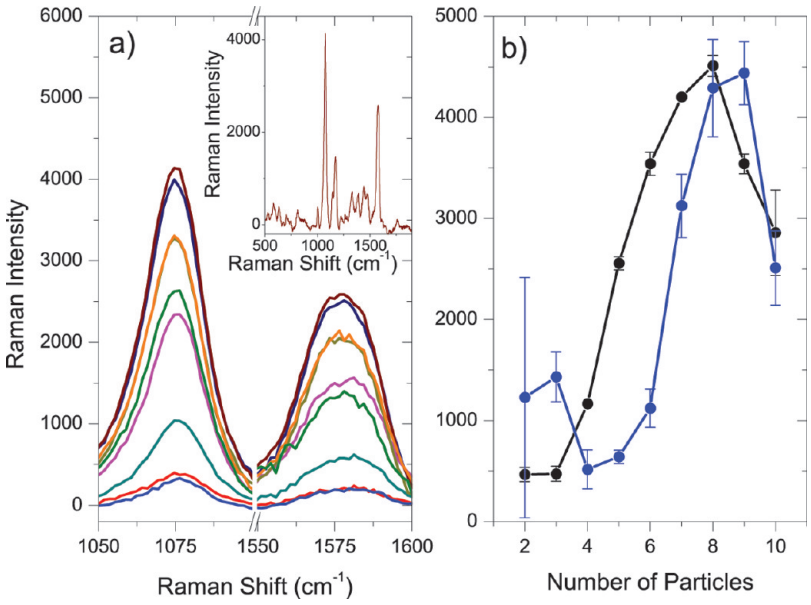

Figure 7. (a) Experimental SERS spectra of 1077 and 1590 cm^{-1} modes of pMA on dimer and nanoplasmonic necklaces of varying particle numbers (red, dimer; blue, triangle; cyan, square; pink, pentagon; yellow, hexagon; navy, heptagon; maroon, octagon; orange, nonagon; green, decagon). Inset figure shows full SERS spectrum from 500 to 2000 cm^{-1} of an octagon necklace. (b) Experimental Raman intensities of the 1077 cm^{-1} mode as a function of number of particles (black line) and calculated enhancement factors from FDTD analysis (blue line).

near-field intensity enhancement for necklaces as a function of the diameter of the necklaces. The maximum near-field intensity is probed over the entire simulation boundary within a plane bisecting the cylinders and over a wavelength range from 600 to 1600 nm. This maximum intensity is then averaged at the optimal wavelength over different polarization angles in the range 0−180° in 5° increments. As a result, the error bars shown in Figure 6a indicate the standard deviation in the intensity enhancement sampled at various polarization angles and give a measure of the robustness of the near-field optimization with respect to the input polarization state. The necklace diameter in Figure 6a is considered as the maximum center-to-center distance between particles in these necklace configurations. Figure 6a shows a principal peak in the 200−600 nm necklace diameter range and a less intense, secondary peak in the 1200−1600 nm range. These local maxima were linearly interpolated by the two dashed lines shown in Figure 6a.

The relevance of photonic−plasmonic coupling is clearly revealed in Figure 6b, where we plot the wavelengths of peak intensity enhancement (polarization averaged as before) *versus* the necklace diameter. The dashed lines in Figure 6b show an approximate linear relationship between the peak wavelength and the necklace diameter. This behavior is evidence of photonic modes being diffracted into the necklace plane and can be characterized by the equation $\lambda = (nD/N)$, where D is the necklace diameter, n is the refractive index of the substrate, and N is the mode order.[27] The slope of the $N = 1$ mode is 1.32, while the $N = 2$ slope is 0.65. The data in Figure 6 demonstrate that, within a scaling factor of approximately 1.3, photonic diffraction and light trapping occur for necklace diameters approximately equal to an integer multiple of the resonance wavelength. As a result, this strong photonic−plasmonic coupling provides a simple design rule for the optimal necklace geometries for each particle size, which can be simply designed to produce the maximum near-field intensities.

In the next section, we will experimentally demonstrate our necklace optimization using SERS signals as probes of the local near-fields.

Surface-Enhanced Raman Scattering. Surface-enhanced Raman scattering is a technique used to fingerprint the vibrational structure of a particular analyte. Raman scattering is an inelastic light-scattering process wherein incident light interacts with vibrational states of an active object (*i.e.*, a molecule, a crystal, *etc.*), causing the scattered light to shift in frequency to lower energy (Stokes-shifted component) and to higher energy (anti-Stokes-shifted component) with respect to the elastic component.[29] SERS is a well-established and reliable method for label-free chemical and biological sensing[20,30] and has detected signals down to the single-molecule limit.[31] Recently, structural enhancement of SERS signals has been demonstrated on engineered arrays of metal nanoparticles such as deterministic aperiodic nanostructures[32] and nanocluster arrays[33] to exhibit enhancement factors from 10^5 to 10^7. Since Raman enhancement scales roughly as the fourth power of the local field, we can use SERS as a qualitative tool to characterize the near-field properties of nanoplasmonic necklaces.

In Figure 7a we show the Raman spectra of *p*-mercaptoaniline (pMA) monolayers collected on Au nanoplasmonic necklaces of varying particle number, as well as on nanoparticle dimer arrays. The dominant Stokes modes of pMA are evident in all of the spectra (1077 and 1590 cm^{-1}).[34] We can see in Figure 7 that when particles are added to the necklace, the intensity of both Stokes modes increases significantly. Focusing on the 1077 cm^{-1} mode, we present in Figure 7b the Raman intensity collected on each nanoplasmonic necklace as a function of the number of particles in the necklace. This clearly demonstrates the role of the number of particles in the Raman signal of the 1077 cm^{-1} mode, which is driven by the local plasmonic fields enhanced by the photonic−plasmonic coupling mechanism discussed above. In order to demonstrate this, we also plot in Figure 7b the calculated local (*i.e.*, near-field) intensity scaling obtained by FDTD (blue) and compared directly with the trend in the SERS data (black). Calculations were obtained using the equation $|E(\lambda_{ex})|^2|E(\lambda_s)|^2$,[2,17] and they show qualitatively good agreement with SERS measurements, which demonstrates the necklace optimization on the near-fields. We also notice that the calculations were obtained using normal incident light, which can explain the discrepancies with the measured data. From the data and the simulations presented in Figure 7, it is clear that nanoplasmonic necklaces represent a significant advancement over the vastly utilized particle dimer configuration.

CONCLUSIONS

In this work, we have computationally and experimentally investigated the far-field scattering and near-field localization properties of nanoplasmonic necklaces consisting of Au nanocylinders arranged in circular loops of varying particle numbers. We demonstrate that particle necklaces represent a fully engineerable plasmonic platform that offers a simple strategy for the design of enhanced near-fields on planar substrates. Moreover, we demonstrate that nanoplasmonic necklaces can easily be optimized by choosing their diameters to be an integer multiple of the wavelength, leading to strong photonic−plasmonic coupling effects that boost their near-field intensities. Our analysis is supported by dark-field scattering spectroscopy and SERS measurements performed on pMA molecular monolayers, demonstrating the optimization of the near-fields in nanoplasmonic necklaces and their superior performances, compared to conventional nanoparticle monomer and dimer arrays.

METHODS

Nanoplasmonic Necklace Fabrication. Nanoplasmonic necklaces were fabricated using electron-beam lithography (EBL) patterning of a 180 nm coating of poly(methyl methacrylate) 950 resist on a fused silica substrate soft baked at 180 °C in an oven for 20 min. We make use of a sacrificial 10 nm Au coating to eliminate electron-beam charging of the substrate while writing with a Zeiss SUPRA 40VP SEM equipped with a Raith beam blanker and NPGS nanopatterning software. Development took place in methyl isobutyl ketone diluted in 2-propanol. Then 28 nm of Au was deposited on top of a 2 nm Ti adhesion layer using electron-beam evaporation. Liftoff was performed by sonicating the samples in acetone.

Finite-Difference Time-Domain Method. In our FDTD analysis, the nanocylinders have a diameter of 150 nm, minimum edge-to-edge separation of 25 nm, and height of 30 nm, which we found optimal for near-infrared sensing.[12,32] Their material dispersion properties are modeled using the Johnson and Christy data.[35] The grid size surrounding the gold nanoparticles is 2.5 nm in the *x* and *y* (in-plane) dimensions and 2 nm in the *z* (out-of-plane) dimension to ensure numerical convergence. The necklaces are simulated on a glass substrate of index $n = 1.45$ in order to exactly describe our experimental conditions. In all simulations, plane wave excitation was used at normal incidence to the substrate. Perfectly matched layer (PML) boundary conditions were used to ensure absorption of electromagnetic radiation at the simulation boundaries.[36] Twelve PML layers are used to minimize reflections from the boundary; the normalized maximum absorption coefficient, σ, is 0.25 and set to increase cubically as fields propagate through the PML layers. The simulations were performed using the commercial software Lumerical FDTD Solutions.[37]

Dark-Field Spectroscopy. All experimental dark-field spectra were collected using an upright Olympus microscope (BX51WI) with unpolarized, incoherent, white light halogen source excitation. A dark-field condenser (NA = 1.2 to 1.4) was used to couple our excitation to the sample at a high angle, with a pinhole of 2 mm diameter placed before the condenser to limit the incident *k*-vectors and improve the overall spectral resolution. Index-matching fluid was used to couple the condenser to the sample substrate. The collection used was a 10× objective with NA 0.25. The data were collected using a grating spectrometer and CCD (Andor Shamrock SR303i) electrically cooled to −75 °C. Spatial filtering at the CCD was used for background noise reduction and to ensure that signal was obtained from only one array of nanoplasmonic necklaces. All the scattering spectra were background corrected by subtraction of the scattering signal from an equal-size, unpatterned area adjacent to each array. The scattering spectra were then normalized by dividing the background-corrected spectra to the emission line shape of the excitation lamp.

SERS Detection. Nanoplasmonic necklace samples were fabricated as previously discussed, incubated in ethanol with a 10 mM concentration of pMA to form a self-assembled monolayer on top of the necklace arrays, and rinsed in pure ethanol before measurement. The sample arrays were excited by a diode laser with 785 nm wavelength and 20.5 mW output power that was fiber coupled to a 40× objective (NA = 0.65) through an upright Olympus microscope. The backscattered signal was sent to an electrically cooled CCD as in the dark-field scattering measurements above. Frequency calibration was performed by referencing the 520 cm^{-1} line of silicon. All spectra were averaged over 10 measurements with a 2 s integration time. The laser spot size was constant in all measurements to ensure consistency between experimental data.

Acknowledgment. This work was partially supported by the ARL Cooperative Agreement (No. W911NF-06-2-0040) and by the NSF (No. CBET-0853798).

REFERENCES AND NOTES

1. Maier, S. A. *Plasmonics: Fundamentals and Applications*, 1st ed.; Springer: Berlin, 2007.

2. Genet, C.; Ebbesen, T. W. Light in Tiny Holes. *Nature* **2007**, *445*, 39–46.
3. Fan, J. A.; Wu, C.; Bao, K.; Bao, J.; Bardhan, R.; Halas, N. J.; Manoharan, V. N.; Nordlander, P.; Shvets, G.; Capasso, F. Self-Assembled Plasmonic Nanoparticle Clusters. *Science* **2010**, *328*, 1135–1138.
4. Gopinath, A.; Boriskina, S. V.; Feng, N.-N.; Reinhard, B. M.; Dal Negro, L. Photonic- Plasmonic Scattering Resonances in Deterministic Aperiodic Structures. *Nano Lett.* **2008**, *8*, 2423–2431.
5. Forestiere, C.; Donelli, M.; Walsh, G. F.; Zeni, E.; Miano, G.; Dal Negro, L. Particle-Swarm Optimization of Broadband Nanoplasmonic Arrays. *Opt. Lett.* **2010**, *35*, 133–135.
6. Hao, E.; Schatz, G. C. Electromagnetic Fields Around Silver Nanoparticles and Dimers. *J. Chem. Phys.* **2004**, *120*, 357–366.
7. Tripathy, S.; Marty, R.; Lin, V. K.; Teo, S. L.; Ye, E.; Arbouet, A.; Saviot, L.; Girard, C.; Han, M. Y.; Mlayah, A. Acousto-Plasmonic and Surface-Enhanced Raman Scattering Properties of Coupled Gold Nanospheres/Nanodisk Trimers. *Nano Lett.* **2011**, *11*, 431–437.
8. Rycenga, M.; Camargo, P. H. C.; Li, W.; Moran, C. H.; Xia, Y. Understanding the SERS Effects of Single Silver Nanoparticles and Their Dimers, One at a Time. *J. Phys. Chem. Lett.* **2010**, *1*, 696–703.
9. Fan, J. A.; Bao, K.; Wu, C.; Bao, J.; Bardhan, R.; Halas, N. J.; Manoharan, V. N.; Shvets, G.; Nordlander, P.; Capasso, F. Fano-Like Interference in Self-Assembled Plasmonic Quadrumer Clusters. *Nano Lett.* **2010**, *10*, 4680–4685.
10. Hao, F.; Nehl, C. L.; Hafner, J. H.; Nordlander, P. Plasmon Resonances of a Gold Nanostar. *Nano Lett.* **2007**, *7*, 729–732.
11. Trevino, J.; Cao, H.; Dal Negro, L. Circularly Symmetric Light Scattering from Nanoplasmonic Spirals. *Nano Lett.* **2011**, *11*, 2008–2016.
12. Gopinath, A.; Boriskina, S. V.; Premasiri, W. R.; Ziegler, L.; Reinhard, B. M.; Dal Negro, L. Plasmonic Nanogalaxies: Multiscale Aperiodic Arrays for Surface-Enhanced Raman Sensing. *Nano Lett.* **2009**, *9*, 3922–3929.
13. Gunnarsson, L.; Bjerneld, E. J.; Xu, H.; Petronis, S.; Kasemo, B.; Käll, M. Interparticle Coupling Effects in Nanofabricated Substrates for Surface-Enhanced Raman Scattering. *Appl. Phys. Lett.* **2001**, *78*, 802–804.
14. Lassiter, J. B.; Sobhani, H.; Fan, J. A.; Kundu, J.; Capasso, F.; Nordlander, P.; Halas, N. J. Fano Resonances in Plasmonic Nanoclusters: Geometrical and Chemical Tunability. *Nano Lett.* **2010**, *10*, 3184–3189.
15. Aćimović, S. S.; Kreuzer, M. P.; González, M. U.; Quidant, R. Plasmon Near-Field Coupling in Metal Dimers as a Step toward Single-Molecule Sensing. *ACS Nano* **2009**, *3*, 1231–1237.
16. Li, W.; Camargo, P. H. C.; Lu, X.; Xia, Y. Dimers of Silver Nanospheres: Facile Synthesis and Their Use as Hot Spots for Surface-Enhanced Raman Scattering. *Nano Lett.* **2009**, *9*, 485–490.
17. Banaee, M. G.; Crozier, K. B. Mixed Dimer Double-Resonance Substrates for Surface- Enhanced Raman Spectroscopy. *ACS Nano* **2011**, *5*, 307–314.
18. Yoon, D.; Moon, H.; Son, Y.-W.; Samsonidze, G.; Park, B. H.; Kim, J. B.; Lee, Y.; Cheong, H. Strong Polarization Dependence of Double-Resonant Raman Intensities in Graphene. *Nano Lett.* **2008**, *8*, 4270–4274.
19. Ming, T.; Zhao, L.; Yang, Z.; Chen, H.; Sun, L.; Wang, J.; Yan, C. Strong Polarization Dependence of Plasmon-Enhanced Fluorescence on Single Gold Nanorods. *Nano Lett.* **2009**, *9*, 3896–3903.
20. Moskovits, M. Surface-Enhanced Spectroscopy. *Rev. Mod. Phys.* **1985**, *57*, 783–826.
21. Yan, B.; Boriskina, S. V.; Reinhard, B. M. Optimizing Gold Nanoparticle Cluster Configurations (n = 7) for Array Applications. *J. Phys. Chem. C* **2011**, *115*, 4578–4583.
22. Mirin, N. A.; Bao, K.; Nordlander, P. Fano Resonances in Plasmonic Nanoparticle Aggregates. *J. Phys. Chem. A* **2009**, *113*, 4028–4034.
23. Alegret, J.; Rindzevicius, T.; Pakizeh, T.; Alaverdyan, Y.; Gunnarsson, L.; Käll, M. Plasmonic Properties of Silver Trimers with Trigonal Symmetry Fabricated by Electron-Beam Lithography. *J. Phys. Chem. C* **2008**, *112*, 14313–14317.
24. Hentschel, M.; Saliba, M.; Vogelgesang, R.; Giessen, H.; Alivisatos, A. P.; Liu, N. Transition from Isolated to Collective Modes in Plasmonic Oligomers. *Nano Lett.* **2010**, *10*, 2721–2726.
25. Hentschel, M.; Dregely, D.; Vogelgesang, R.; Giessen, H.; Liu, N. Plasmonic Oligomers: The Role of Individual Particles in Collective Behavior. *ACS Nano* **2011**, *5*, 2042–2050.
26. Kettle, S. *Symmetry and Structure: Readable Group Theory for Chemists*; John Wiley, 2007.
27. Félidj, N.; Laurent, G.; Aubard, J.; Lévi, G.; Hohenau, A.; Krenn, J. R.; Aussenegg, F. R. Grating-Induced Plasmon Mode in Gold Nanoparticle Arrays. *J. Chem. Phys.* **2005**, *123*, 221103.
28. Chu, Y.; Banaee, M. G.; Crozier, K. B. Double-Resonance Plasmon Substrates for Surface- Enhanced Raman Scattering with Enhancement at Excitation and Stokes Frequencies. *ACS Nano* **2010**, *4*, 2804–2810.
29. Ru, E. L.; Etchegoin, P. *Principles of Surface-Enhanced Raman Spectroscopy: And Related Plasmonic Effects*; Elsevier, 2008.
30. Willets, K. A.; Van Duyne, R. P. Localized Surface Plasmon Resonance Spectroscopy and Sensing. *Annu. Rev. Phys. Chem.* **2007**, *58*, 267–297.
31. Doering, W. E.; Nie, S. Single-Molecule and Single-Nanoparticle SERS: Examining the Roles of Surface Active Sites and Chemical Enhancement. *J. Phys. Chem. B* **2002**, *106*, 311–317.
32. Gopinath, A.; Boriskina, S. V.; Reinhard, B. M.; Dal Negro, L. Deterministic Aperiodic Arrays of Metal Nanoparticles for Surface-Enhanced Raman Scattering (SERS). *Opt. Express* **2009**, *17*, 3741–3753.
33. Yan, B.; Thubagere, A.; Premasiri, W. R.; Ziegler, L. D.; Dal Negro, L.; Reinhard, B. M. Engineered SERS Substrates with Multiscale Signal Enhancement: Nanoparticle Cluster Arrays. *ACS Nano* **2009**, *3*, 1190–1202.
34. Jackson, J. B.; Halas, N. J. Surface-Enhanced Raman Scattering on Tunable Plasmonic Nanoparticle Substrates. *Proc. Natl. Acad. Sci.* **2004**, *101*, 17930–17935.
35. Johnson, P. B.; Christy, R. W. Optical Constants of the Noble Metals. *Phys. Rev. B* **1972**, *6*, 4370–4379.
36. Berenger, J.-P. A Perfectly Matched Layer for the Absorption of Electromagnetic Waves. *J. Comput. Phys.* **1994**, *114*, 185–200.
37. Lumerical Solutions, Inc. http://www.lumerical.com/.